Hindawi
Journal of Nanomaterials
Volume 2022, Article ID 2430840, 15 pages
https://doi.org/10.1155/2022/2430840

*Research Article*

# Solar Power Light-Driven Improved Photocatalytic Action of Mg-Doped CuO Nanomaterial Modified with Polyvinylalcohol

**A. Mohamed Azharudeen**,[1] **A. Mohamed Ismail Badhusha**,[2] **Mohd Shahnawaz Khan**,[3] **S. Arun Prabhu**,[4] **P. Vijaya Kumar**,[5] **R. Karthiga**,[6] **Hamza A. Odeibat**,[3] **Huma Naz**,[7] **K. Buvaneswari**,[8] **and Md. Rabiul Islam**[9]

[1]*Department of Chemistry, M.S.S. Wakf Board College, Madurai 625020, Tamil Nadu, India*
[2]*Research Department of Chemistry, Sadakathullah Appa College, Tirunelveli 627011, Tamil Nadu, India*
[3]*Department of Biochemistry, College of Sciences, King Saud University, Riyadh, Saudi Arabia*
[4]*Department of Chemistry, National College (Autonomous), Tiruchirappalli 620001, Tamil Nadu, India*
[5]*Department of Chemistry, Jairams Arts and Science College, Karur 639003, Tamil Nadu, India*
[6]*PG & Research Department of Chemistry, C.P.A. College, Bodinayakanur 625513, Tamil Nadu, India*
[7]*Department of Medicine, University of Missouri, Columbia, Missouri 65201, USA*
[8]*PG Department of Chemistry, Sri S. Ramasamy Naidu Memorial College, Sattur 626203, Tamil Nadu, India*
[9]*Department of Pharmacy, University of Asia Pacific, Dhaka, Bangladesh*

Correspondence should be addressed to A. Mohamed Azharudeen; azhar5406@gmail.com
and Md. Rabiul Islam; robi.ayaan@gmail.com

Received 11 February 2022; Accepted 25 February 2022; Published 14 March 2022

Academic Editor: Palanivel Velmurugan



Sonochemical synthesis was used to create novel solar light active Mg-doped CuO nanoparticles. Through a chemical impregnation method, the produced nanomaterial was changed with PVA (polyvinylalcohol). The optical properties, crystal structure, and surface morphologies of the synthesized nanomaterials were probed by UV-visible spectroscopy (UV-vis-DRS), Fourier transform infrared spectroscopy (FT-IR), Raman spectroscopy, X-ray diffraction (XRD), scanning electron microscopy (SEM), high-resolution transmission electron microscopy (HR-TEM), energy-dispersive X-ray spectroscopy (EDX), X-ray photoelectron spectroscopy (XPS), photoluminescence spectroscopy (PL), thermogravimetric analysis (TGA), and BET specific surface area studies. The prepared nanomaterials were utilized for the photocatalytic destruction of methylene blue (MB). The photocatalytic activity of PVA-modified Mg-doped CuO nanocomposite is magnificent to CuO and Mg-doped CuO nanomaterials. This is because of the remarkable electron-hole dissociation and overwhelming increased photocatalytic activity achieved through surface modification. Additionally, the consequence of several reaction factors like pH, catalyst dosage, and MB concentration was deliberated. This research could lead to the development of polymer-based metal oxide-doped catalysts for the decomposition of organic contaminants in wastewater.

## 1. Introduction

Nanotechnology has resulted in the creation of a variety of tiny materials. Nanoparticles are a broad category of materials that include particulate substances with a minimum diameter of 100 nm. In recent years, nanotechnology has grown across all fields of science and technology including engineering, medicine, pharmaceuticals, agriculture, and the environment. Among the many general uses of nanotechnology, the usage of nanomaterials in cosmetics, sunscreens, surface coatings, environmental remediation, and some food products is an example of successful application [1, 2]. Several applications using nanomaterials have been reported in the past decades. At present, environmental pollution, in particular, harms human health, causing damage to the liver and kidneys, as well as diarrhea, encephalitis, stomach cramps,

vomiting, and respiratory infections. Water contamination, excretion of harmful organic pollutants from chemicals, coating, paper printing, pharmaceutical, leather, pulp, dyeing, and textile industries are common examples of environmental pollution [3–7]. These organic pollutants can be degraded using semiconductor photocatalysts [8] and transformed to $CO_2$, $H_2O$, and other tiny molecules [9], which do not change the environmental situation. For example, Abbasi-Asl et al. published a heterostructure photocatalyst for organic pollutant degradation utilizing solar light, while Oliveira et al. described $TiO_2$ nanoparticles for organic dye degradation. A plethora of studies on the breakdown of organic contaminants have been proposed [10–13]. Furthermore, standard procedures for the removal of organic contaminants from the water will be developed to ensure that the environment is pollution-free.

Semiconductor-based nanocomposites have recently piqued interest in a variety of scientific and technological domains [14–17]. CuO and its composites have emerged as a viable candidate in the field of photocatalysis among semiconductor materials. It has a small band gap energy of 1.2–1.6 eV, as well as stable, abundant, nontoxic, and economical physical and chemical features [18–20]. It has potential uses in technology such as energy conversion, environmental remediation, sensors, photocatalysts, solar cells, and optical devices [21, 22]. Several investigations on CuO as a photocatalyst have been conducted in the previous decade [23]. For example, Sahu et al. [24] described an Au-CuO hybrid material for methylene blue degradation, while Raina et al. [25] discussed the synthesis of Cu nanoparticles for the same. Copper oxide nanoparticles have also been employed in plenty of applications with solar energy conversion, $CO_2$ reduction, and solar cells [26–28].

Furthermore, nanoparticles produced from copper oxide have sparked numerous curiosity in the dissemination of photocatalysis. Sun et al. [29], for example, reported Mg/$CuO/Fe_2O_3$ heterogeneous catalysts for the dissociation of organic pollutants, Mg acting a predominant part in the destruction of organic pollutants in this work. Since then, it has aided in the development of morphological structure, high crystallinity, catalytic ability, oxygen vacancy, and storage. Selvam et al. [30] also explained why Mg-doped ZnO photocatalysts function so well. As a result, a Mg-doping catalyst could be a good way to boost the performance of CuO nanoparticles in photocatalysts. Despite various Mg-doped semiconductors having been described for the damage of organic pollutants, polymer-based nanocomposites for the demolition of organic dyes have attracted a lot of attention [31] because polymers are adjustable in size, shape, chemical structure, ordered nanoparticle assembly, biocompatible, electron promoter, and low in cost [32, 33]. To construct the nanocomposites for the dissociation of organic compounds like PVA (polyvinylalcohol) [34, 35], chitosan [36, 37], and cellulose [33, 38, 39], a suitable number of natural and synthetic hydrophilic polymeric materials were utilized. Among the hydrophilic material, PVA is a hydrophilic polymer that is nontoxic, inexpensive, readily available, and biocompatible, has excellent thermal strength, is water soluble, can produce fine flexible films, and has been described to have noble photocatalytic activity in wastewater management [32, 40–42]. As a result, the PVA-modified CuO-Mg composite has outstanding metal-doped metal oxide and polymer properties and so could be a smart, promising composite for effective photocatalysts.

In this work, CuO-Mg nanoparticles were produced using a sonochemical technique and then modified with PVA. The efficiency of photocatalytic movement of manufactured nanomaterials was investigated under solar light illumination. With remarkable reusability, the CuO/Mg/PVA composite may achieve effective catalysis and continuous photodegradation of organic dye.

## 2. Materials and Methods

*2.1. Reagents.* Magnesium chloride hexahydrate ($MgCl_2.6H_2O$), copper(II) nitrate trihydrate ($Cu(NO_3)_2.3H_2O$), sodium hydroxide, and polyvinylalcohol (PVA, MW = 67000) were obtained from Spectrum Chemicals, India. Methylene blue (MB) was brought from Merck Chemicals, India. All the chemicals were of analytical grade and employed as received without refinement. Double distilled (DD) water was used during the experiment.

*2.2. Sonochemical Synthesis of Mg-Doped CuO (MC) Nanoparticles.* The sonochemical approach was used to make magnesium-doped copper oxide nanoparticles. Separately, 2.41 g of $Cu(NO_3)_2.3H_2O$ and 1.01 g of $MgCl_2.6H_2O$ were dissolved in 100 mL of DD water, and the solution was well mixed and agitated for 10-15 min using a magnetic stirrer. 0.4 g NaOH was dissolved in 100 mL DD water and dropped into the aforementioned solution drop by drop. The resulting solution was treated with ultrasound for 1 hour at room temperature, using a titanium-made high-intensity ultrasonic horn probe sonicator and modifying the ultrasound frequency (20 kHz and 100 $W/cm^2$). The resultant black precipitate was separated using centrifugation after the irradiation procedure and washed with water and ethanol and dried at 80°C for 1 hour. The final product was calcined for 1 hour at 400°C. In the absence of MgCl.$6H_2O$, copper oxide nanoparticles were also produced using a similar approach.

*2.3. Preparation of Mg-CuO-PVA (MCP) Nanocomposite.* Mg-CuO-PVA nanocomposite was synthesized by simple chemical impregnation method. 2 g of previous synthesized Mg-CuO nanoparticle in 100 mL of ethanol was blended with 2 g of PVA in 100 mL ethanol by ultrasonication for 1 hr. After 12 hrs of stirring, the solvent was left, and the product was dried at 80°C and heat treatment at 120°C in a hot air oven for 2 hrs.

*2.4. Measurement.* The functional group was determined using JASCO FT/IR-4200 spectroscopy, and the optical property of produced nanocomposites was measured using a JASCO V-750 spectrophotometer. The Raman spectrum was created by a 532 nm LabRAM HR evolution Raman spectrometer. XPERT PRO X-ray with Cu K radiation of wavelength 1.541 was employed to investigate the crystalline phase of produced nanomaterials. Using a JOEL model JSM 6701FSEM, the SEM-EDX outcome of produced

nanocomposites was investigated. HR-TEM pictures were captured using a JOEL 3010 microscope. FLUROCUBE-JOBIN YVON spectrofluorometer fluorolog-3 with 450 W xenon lamp is utilized photoluminescence (PL) research. TGA was analyzed using a TGA-50 SHIMADZU analyzer in the range of 1 to 1000°C at 5°C/min in $N_2$ atmosphere. Micromatrics, ASAP 2020 BET instrument, was employed to find the surface area, and XPS measurement was recorded by AXIS-NOVA system. A JASCO V-530 UV/VIS spectrometer was used to study the absorbance spectrum.

*2.5. Photocatalytic Activity Measurement.* The photocatalytic actions of manufactured nanomaterials in the decoloration of methylene blue (MB) dye under sunshine were examined. In this experiment, 300 mL of 20 $\mu$M MB solution was used to disperse 0.2 g of produced nanomaterials. The resulting mixture was agitated in a slutty type batch reactor for 15 minutes in the dark to accomplish an adsorption-desorption equilibrium before being illuminated with sunlight. The degradation of MB dye was measured regularly by centrifuging a 5 mL sample of the reaction mixture. The supernatant solution was inspected by a UV-vis spectrometer. The consistent degradation of MB was studied by illumination time, catalyst dosage, and initial concentration of MB dye.

The decoloration of the dye from the solution was estimated using the following relation.

$$\text{Photodegradation\%of dye} = \frac{C_o - C}{C_o} \times 100, \quad (1)$$

where $C_o$ is the dye concentration before illumination and $C$ represents the dye concentration after a certain time illumination.

## 3. Results and Discussion

*3.1. Optical Studies.* The UV-vis-DR spectrographic analysis gives data about the absorption of light. The UV-vis-DR spectra of samples CuO, MC, and MCP are shown in Figure 1. The adsorption edges of CuO, MC, and MCP are displayed at 326.33, 338.41, and 349.86 nm, respectively. The adsorption edges of MC and MCP are shown redshifted due to the surface modifier Mg and PVA. Further, it demonstrates the composite formation with PVA, which can enhance photocatalytic activity.

Moreover, Tauc's plot is employed to investigate the band gap in prepared nanomaterials by following relation (1).

$$\alpha = \frac{C\left(h\nu - E_g\text{bulk}\right)^2}{h\nu}, \quad (2)$$

where $\alpha$, $C$, $h\nu$, and $E_g$bulk are absorption coefficient, constant, photon energy, and band gap, respectively. Figure 1 shows Tauc's plots of CuO, MC, and MCP. The CuO has an optical band gap of 1.84 eV, which is related to its intrinsic band distance. This means that photocatalytic activity is predominantly restricted to the UV light spectrum. Furthermore, the band gap energies for MC and MCP are determined to be 1.23 and 0.67 eV, respectively. As a result, the PVA-incorporated MCP nanocomposite has a small band gap energy and higher optical conductivity than other nanocomposite materials, allowing it to have outstanding photocatalytic activity.

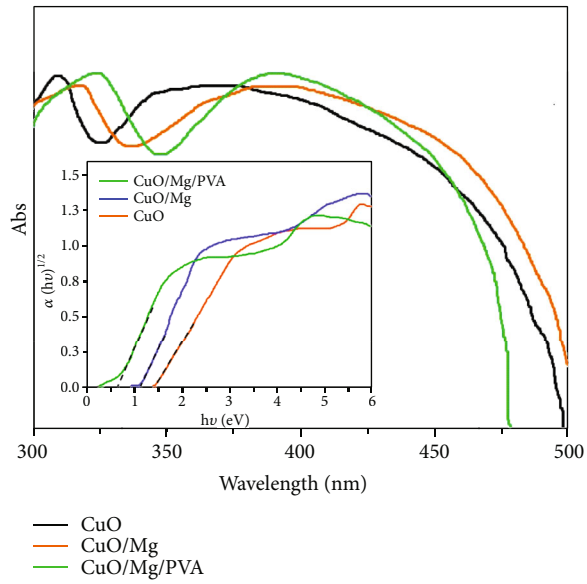


FIGURE 1: UV-vis-DRS of CuO, MC, and MCP nanocomposite. Insert: corresponding Tauc's plots.

*3.2. Fourier Transform Infrared Spectroscopy (FT-IR).* The Cu-O bond formation, presence of hydroxyl group, and moisture content of produced nanomaterials were investigated using an FT-IR spectrum. Figures 2(a)–2(c) demonstrate the FT-IR spectra of prepared undoped CuO nanoparticles, MC, and MCP. CuO's characteristic vibrational bands (Figure 3(a)) appeared at 436.87, 526.21, and 595.32 $cm^{-1}$, which correspond to the monoclinic CuO phase's Cu-O vibrations [43]. This confirmed the creation of CuO nanoparticles, as well as the absence of contaminant peaks in the sample. Similarly, the bands seen in MC (Figure 3(b)) and MCP (Figure 3(c)) samples (425.78, 517.56, and 582.73 $cm^{-1}$) are linked to the Cu-O vibrational frequencies.

Furthermore, the absorption peaks measured at 1144.28, 1465.44, and 2858 $cm^{-1}$ in the FT-IR spectra of MCP nanocomposite are pertained to the C-O, $CH_2$, and C-H groups stretching of PVA, respectively. Furthermore, the wide peak for the O-H stretching mode of PVA exists at 3380.57 $cm^{-1}$ [44–46]. Clearly, the nanocomposite shows a less positive shift in wavenumber in the FT-IR spectrum of MC (Figure 2(b)) and MCP (Figure 2(c)). The doping/capping impact of Mg and PVA on the surface of CuO is triggered by this change. This demonstrates that a CuO-Mg-PVA nanocomposite has formed. The above analysis revealed that no other abnormalities like Mg-O, $Cu_2O$, and $Cu_4O_3$ have been detected in the whole wavelength range describing single phase structure of CuO and

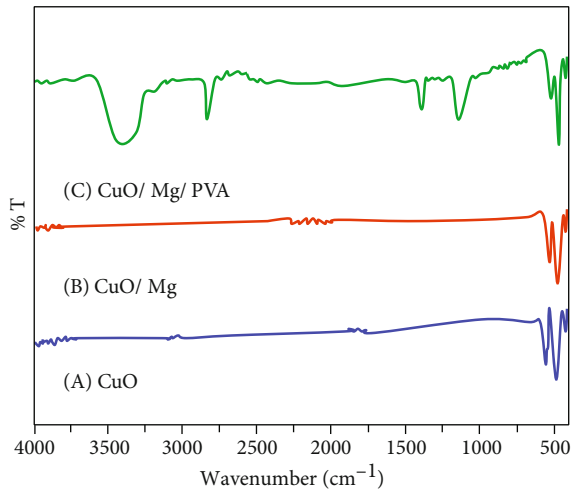


Figure 2: FT-IR spectrum of (a) CuO, (b) MC, and (c) MCP nanocomposites.

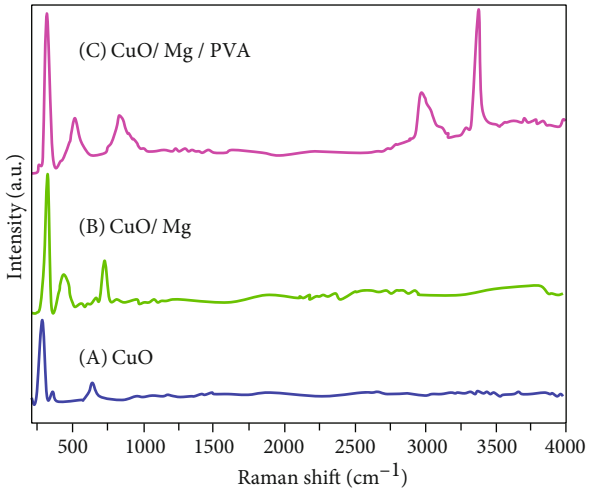


Figure 3: Raman spectrum of (a) CuO, (b) MC, and (c) MCP nanocomposites.

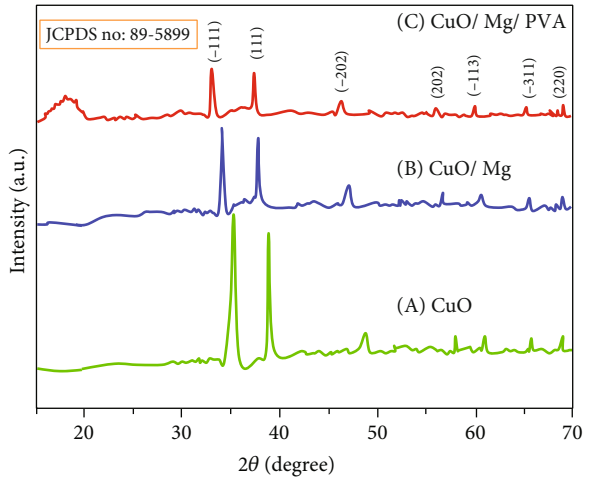


Figure 4: XRD patterns of (a) CuO, (b) MC, and (c) MCP nanocomposites.

effective substitution/modification of Mg ion and PVA on the locations of host CuO.

*3.3. Raman Analysis.* The Raman spectra of CuO, MC, and MCP nanocomposites were presented in Figures 3(a)–3(c). In Figure 3(a), the Raman peaks noticed at 296.44, 342.08, and 630.26 $cm^{-1}$ are related to the Ag, $B_g^1$, and $B_g^2$ mode of CuO [47]. Then, the Raman peaks of MC (Figure 3(b)) were observed at 298.85, 346.21, and 638.48 $cm^{-1}$, and the Raman bands are located at 302.54, 350.67, and 644.83 $cm^{-1}$ in the MCP (Figure 3(c)) sample. The intensity of the Raman peaks expanded in the MC and MCP sample renders to the CuO doped with Mg.

Moreover, the Raman bands situated at 2958.11 and 3420.48 $cm^{-1}$ are pertinent to the stretching mode of C-C and O-H in PVA [48, 49]. This discloses the capping influence of PVA on the surface of CuO-Mg. Further, the Raman bands are red lifted in MC and MCP showing the surface enhancement outcome.

*3.4. Crystal Structure.* The phase structure of synthesized CuO, MC, and MCP nanocomposites was portrayed by XRD pattern and displayed in Figures 4(a)–4(c). The diffraction edges of CuO (Figure 4(a)) acquired at 35.3°, 38.5°, 48.6°, 58.1°, 61.8°, 66.4°, and 68.5° can be assigned to the (-111), (111), (-202), (-113), (-311), and (220) planes of CuO [29] (JCPDS No: 89-5899, phase: monoclinic, lattice: end-centered, a = 4.68, b = 3.42, and c = 5.13). The patterns show no impurity peaks, indicating the cleanliness of the generated CuO samples, and the keen diffraction peaks reveal the magnificent crystal structure of the fabricated CuO. Moreover, as compared to MC (Figure 4(b)) and MCP (Figure 4(c)), the CuO XRD pattern may maintain the normal CuO crystal structure following the incorporation of Mg and PVA.

The intensity of all diffraction peaks appears to be reduced when Mg is doped in MC and MCP. The Mg combines with the CuO structure due to a somewhat lower angle shift in the diffraction peaks. In addition, in sample MCP [43], a large peak was discovered at 18.32°, which corresponded to the crystalline phase of PVA. This validated the presence of PVA on the CuO-Mg nanomaterial's surface. The XRD patterns also reveal that PVA intercalation does not affect the monoclinic phase's crystal structure. Scherrer's formula (1) is used to compute the average crystallite size.

$$D = \frac{K\lambda}{\beta \cos \theta}, \tag{3}$$

where $D$ denotes the average crystallite size, $\beta$ denotes the peak's FWHM, $K$ is the form of a particle factor (it = 0.89), and $\theta$ and $\lambda$ are the incident angle and wavelength of X-rays, correspondingly. CuO, MC, and MCP have typical crystallite diameters of 53.41, 30.78, and 15.16 nm, respectively. During the loading of Mg and PVA, the crystallite size changes slightly. The host CuO is distorted by the doping/capping agent, resulting in a reduction in crystallite size. This demonstrates that Mg and PVA have been incorporated into

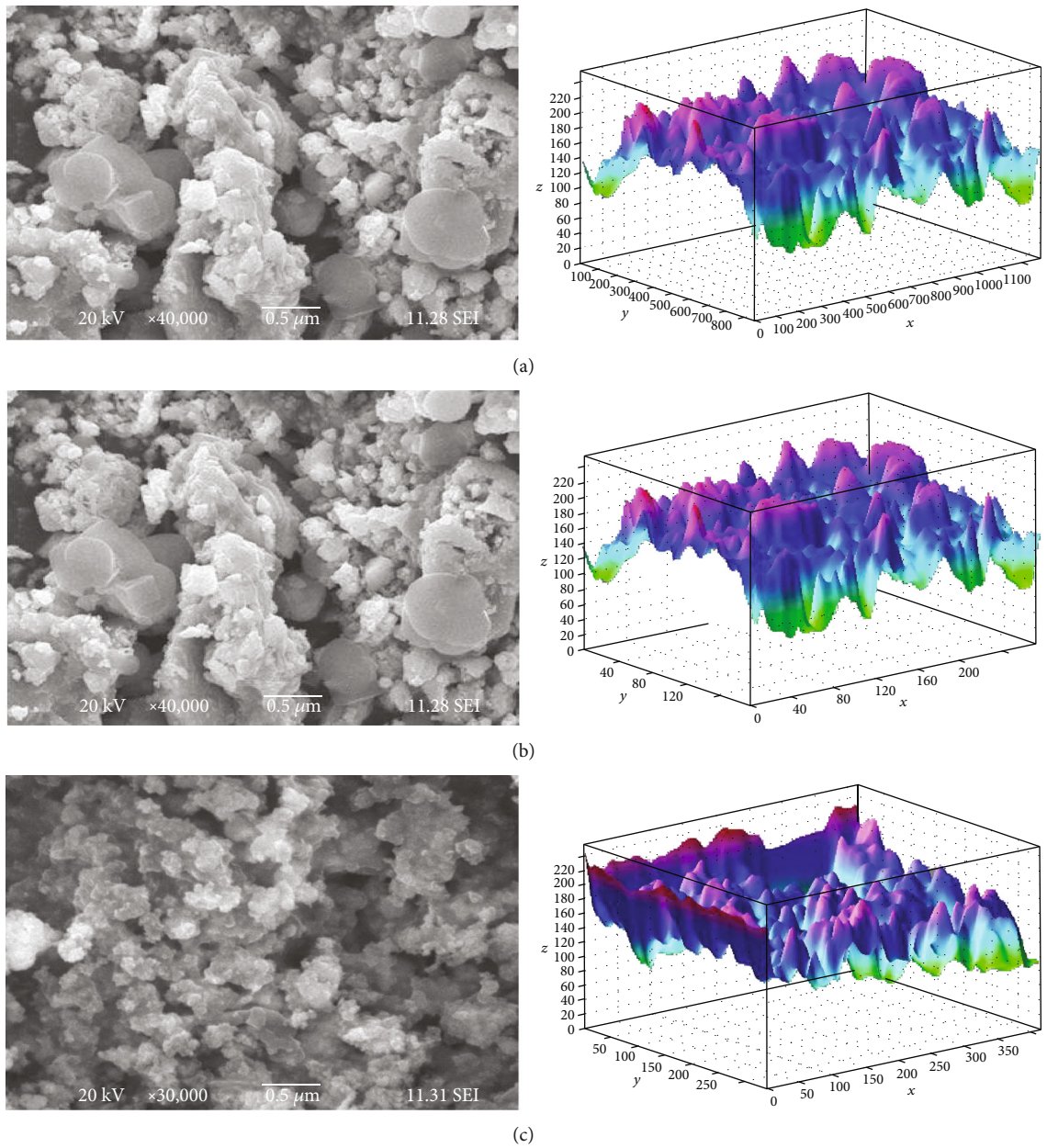


Figure 5: SEM micrograph of (a) CuO, (b) MC, and (c) MCP nanocomposites.

the surface of CuO. As a result, the nanocomposite's construction has been established.

The FT-IR and Raman results are corroborated very well with the XRD result.

*3.5. Morphological Study.* The SEM is used to examine the cryogenically fragmented surfaces of CuO, MC, and MCP, as disclosed in Figures 5(a)–5(c). The CuO SEM picture (Figure 5(a)) demonstrates a larger rod-like structure with a rough surface. The fact that the MC nanoparticle (Figure 5(b)) resembles nanoflakes indicates that CuO has been doped with Mg. However, the MCP nanocomposite (Figure 5(c)) has a shape similar to small hallow nanoflakes, and the MCP is smaller than CuO and MC. This shows that doping/capping is taking place on the surface of CuO. In Figures 5(a) and 5(b), the appropriate interactive 3D surface plots were also shown. MCP has enormous beautiful pores and an energetic surface area that interacts with the analyte, making it stand out among the produced nanocomposite. As a result, the PVA significantly alters the MCP nanocomposite's cryogenically shattered surface. MCP's HR-TEM micrographs (Figures 6(a) and 6(b)) reveal that the nanoparticles are well dispersed within the polymer array. The creation of nanoflakes is confirmed by Figures 6(a) and 6(b). The crystallinity of MCP nanocomposite as observed by a selected region diffraction pattern is shown in

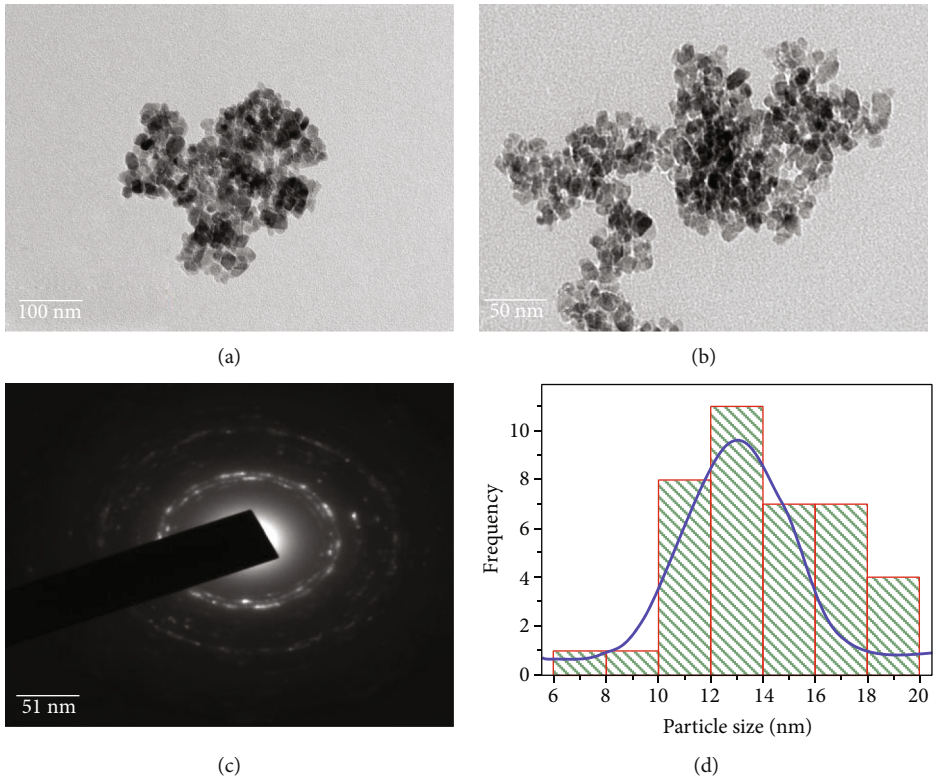


Figure 6: (a and b) HR-TEM images of MCP nanocomposite, (c) SAED image of MCP, and (d) particle size distribution of MCP.

Figure 6(c) (SAED). Those rings are indexed in the stable phase of CuO. The particle distribution of MCP is demonstrated in Figure 6(d). The atom size of the MCP nanocomposite was computed to be 13.94 nm, which is the nearest value to the XRD value.

EDS measurements were used to determine the elemental distributions of the produced nanomaterials. Figures 7(a)–7(c) show the EDS spectra of CuO, MC, and MCP nanocomposites. In the EDS spectrum, the fundamental peaks of Cu and O may be seen. The CuO nanoparticle purity is visible in the uncoated sample. The manufactured nanoparticles have a high stoichiometry and are extremely porous. MCP's very porous surface is an important feature of the photocatalyst. In the EDS spectra of CuO (Figure 7(a)), MC (Figure 7(b)), and MCP (Figure 7(c)), the intensity of Cu increases from 1290.18 to 1493.57 and 2987.72, respectively. This is due to the surface modifier of Mg and PVP enlarging the strength of the Cu. It validates the presence of Mg and PVA on the surface of CuO.

XPS was used to further investigate the surface composition and chemical state of the MCP nanocomposite (XPS). Figures 8(a)–8(c) show the high-resolution XPS spectrum of Cu, Mg, and O. The Cu $2P_{3/2}$ and Cu $2P_{1/2}$ with satellite signals at 942.73 and 944.25 eV are inferable from the presence of Cu(II) [29]. The peaks that appeared in the Cu spectrum (Figure 8(a)) at 933.48 and 953.61 eV are relevant to the Cu $2P_{3/2}$ and Cu $2P_{1/2}$ with satellite signals at 942.73 and 944.25 eV are relevant to the Cu $2P_{1/2}$ with satellite signals. This proves that the phase is CuO rather than $Cu_2O$. Due to the presence of $Mg^{2+}$, Mg 1 s is observed at 1302.78 eV in the XPS spectra of MCP (Figure 8(b)) [50]. On the other hand, the O 1 s region was obtained at 530.96 eV for MCP nanocomposite and illustrated in Figure 8(c). This oxygen energy peak is characteristic of a metal oxide peak [51].

*3.6. Photoluminescence (PL) and Thermogravimetric Analysis (TGA).* The optical properties, crystal structure, and surface morphologies of the synthesized nanomaterials were probed by Raman spectroscopy, X-ray diffraction (XRD), scanning electron microscopy (SEM), high-resolution transmission electron microscopy (HR-TEM), energy-dispersive X-ray spectroscopy (EDX), X-ray photoelectron spectroscopy (XPS), photoluminescence spectroscopy (PL), thermogravimetric analysis (TGA), and BET specific surface area studies.

PL spectroscopy is noteworthy to study the segregation performance of the photogenerated electron-hole pair in a semiconductor nanomaterial. Figure 9 shows PL spectra of CuO, MC and MCP nanocomposites. Two intense peaks at 480.1 and 537.4 nm are noticed and PL intensity is feeble. The diminished fluorescence intensity designates that photoelectrons and holes reunion have been effectively reduced, while increased photocatalytic activity is predicted. With Mg and PVA doping, the PL intensity gradually decreased. This suggests a decreasing rate of electron-hole recombination. In other words, the MCP nanocomposite has a greater separation efficiency of photogenerated electrons and holes than other nanomaterials.

The phase purity was employed by thermal gravimetric measurement. The TG curves of CuO, MC, and MCP are disclosed in Figure 9. The weight loss was observed from

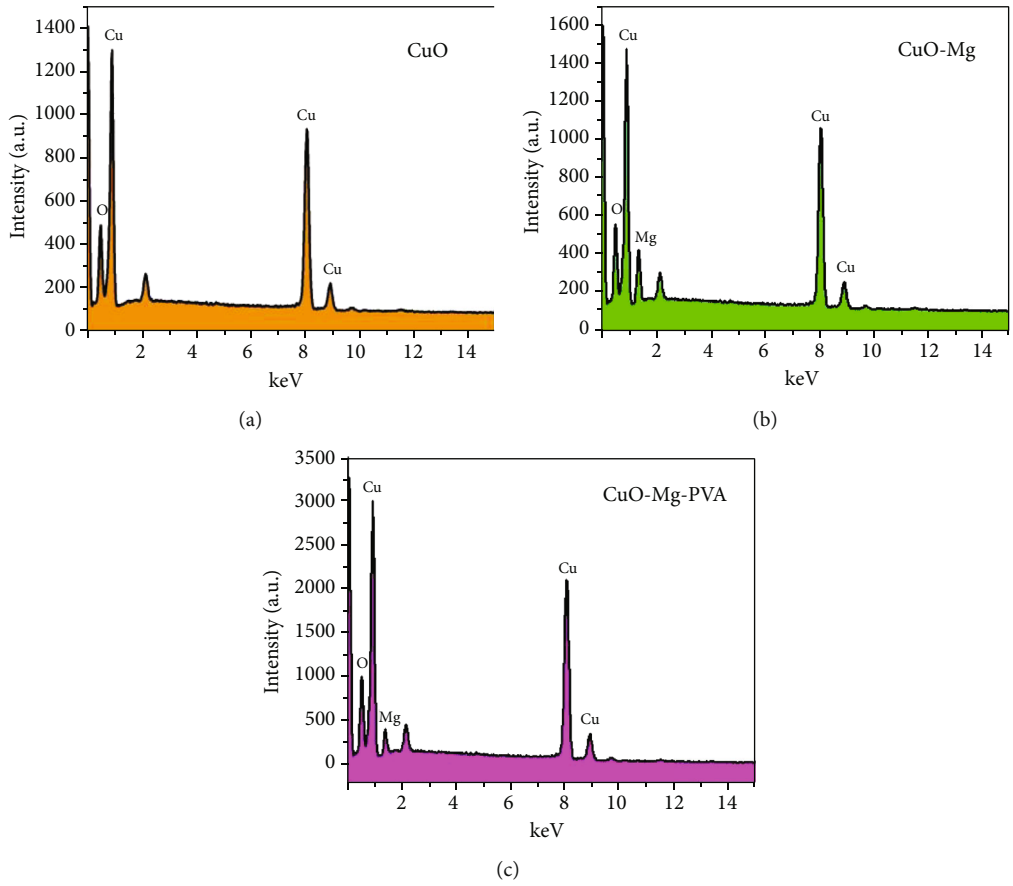


Figure 7: EDS spectrum of (a) CuO, (b) MC, and (c) MCP nanocomposites.

35 to 120°C due to the evaporation of moisture consumed by the nanomaterials. Not all weight loss from 120 to 800°C inferred that no reaction occurred in this range in the TG curve of CuO. After the temperature went beyond 800°C, significant weight loss was monitored in the TG curve by CuO reduction to $Cu_2O$ [52], thus corroborating the formation of CuO nanoparticles. Further, in MC nanoparticles, the small endothermic TG curve is noticed in the range between 310 and 510°C nanoparticles rendering the conversion of Mg into the MgO phase [53]. This demonstrates that the Mg ion has been doped with CuO. The disintegration of PVA is linked to the second and considerable weight loss reported in the range of 200 to 320°C in the TG curve of MCP nanocomposite [54]. The PVA-treated CuO-Mg nanocomposite, on the other hand, shows a significant rising alteration in TGA curves, and the remaining weight shows a significant development in thermal stability. PVA aided CuO-Mg in immobilizing a greater amount of $Cu^{2+}$, resulting in a higher CuO-Mg concentration in the composite photocatalysts. This research demonstrated that PVA loading has an impact on thermal stability.

*3.7. Brunauer-Emmett-Teller (BET).* $N_2$ adsorption-desorption quantification was used to investigate the textural features of powder catalysts. Figures 10(a)–10(c) displayed the $N_2$ adsorption-desorption isotherm analysis of CuO, MC, and MCP. The reversible type-III adsorption isotherm is followed by the prepared CuO nanoparticles (Figure 10(a)). The interaction between $N_2$ gas and CuO (adsorbate-adsorbent) is weak in this case. However, because the tiny pore of CuO does not fill with the adsorbate $N_2$ gas, this type of isotherm is uncommon. The type-V adsorption isotherm curve of MC is shown in Figure 10(b), indicating a poor contact between the adsorbent and adsorbate on the CuO-Mg surface.

The stacking of Mg on copper oxide hints to the development of several porous adsorbents. Accordingly, the surface region was amplified while doping.

Moreover, Figure 10(c) shows type-IV adsorption isotherm curves of MCP. This reveals the individual hysteresis loop and indicates the mesoporous platform of MCP agreeing the IUPAC classification. The structure of nanocomposites has altered from macroporous to mesoporous, as can be noticed. This is because interconnected macroporous allows guest molecules to adsorb by attaching the pore wall locations. CuO, MC, and MCP, respectively, have surface areas of 28.12, 76.67, and 165.43 $m^2/g$. The surface area of MCP nanocomposite increases dramatically when PVA is added. This means that PVA aids in the reduction of polarity in CuO-Mg nanoparticles, resulting in better dispersion and smaller clumps. The formation of aggregates of a few nanoparticles eventually resulted in a surface area increase. Among the synthesized nanomaterials, MCP has a brilliant surface area (165.43 $m^2/g$) and a more dynamic destination

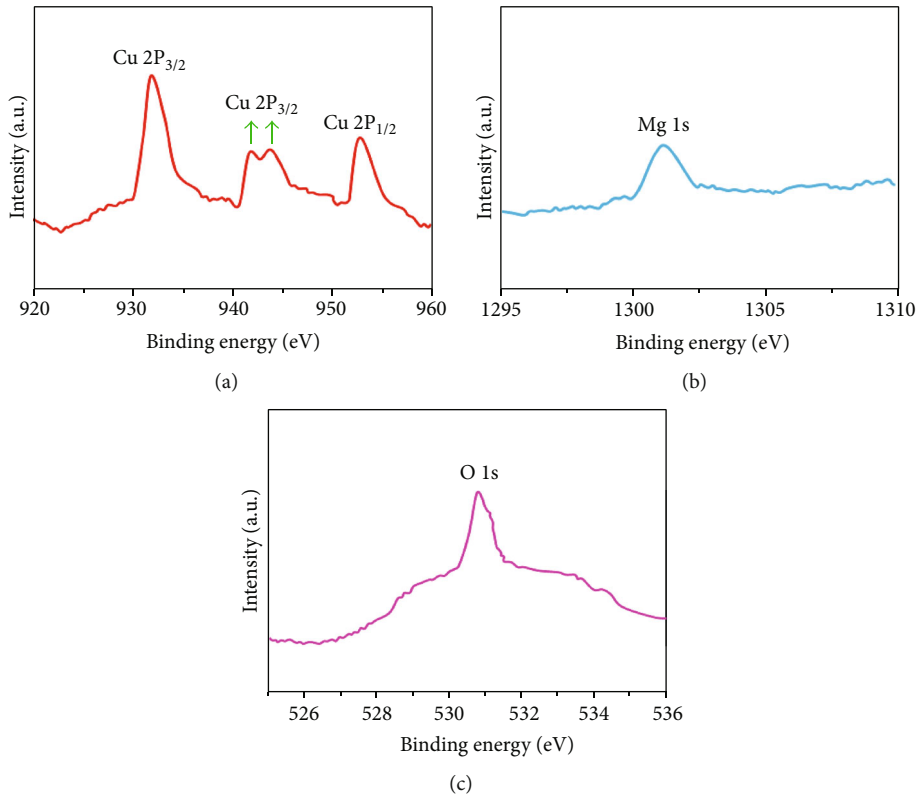


Figure 8: High-resolution XPS spectrum of MCP nanocomposite (a) Cu, (b) Mg, and (c) O.

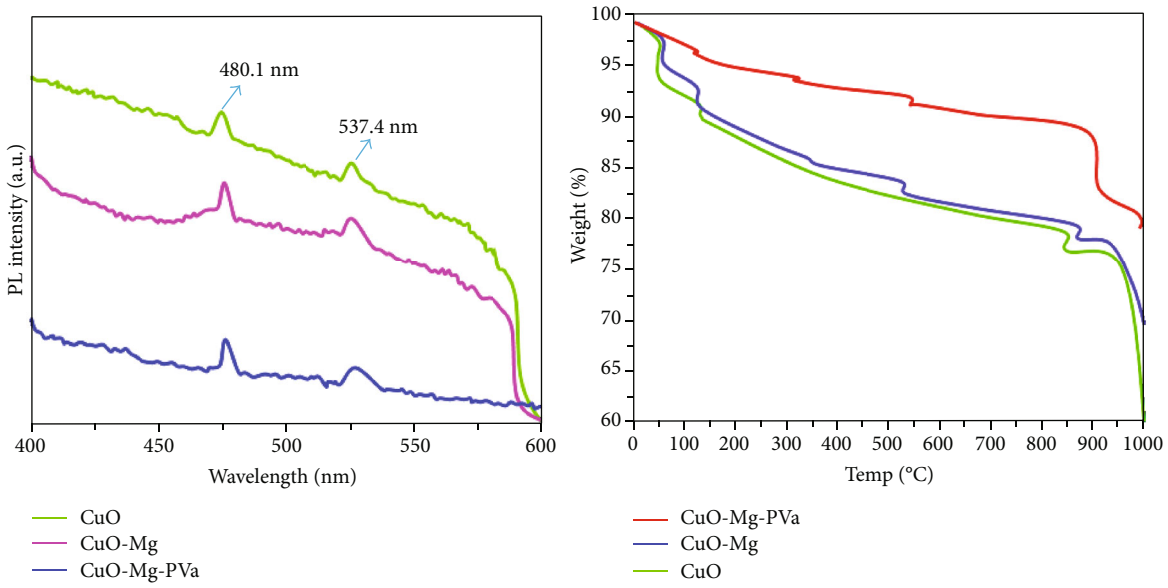


Figure 9: PL spectrum and TGA curves of (a) CuO, (b) MC, and (c) MCP nanocomposites.

given by PVA. It can shows the brilliant and ameliorate character in photocatalytic action [43].

*3.8. Photocatalytic Degradation of Methylene Blue (MB).* Under solar light, photocatalytic measurements of synthesized CuO, MC, and MCP nanocomposite were probed. The photocatalytic decoloration investigation was carried out using catalysts weighing 0.2 g/L, MB concentration of 20 $\mu$M, and an illumination period of 180 minutes. Figures 11(a)–11(c) show the absorption spectrum of CuO, MC, and MCP nanocomposites. From Figures 11(a)–11(c), the sequence of photocatalytic action for the destruction of methylene blue is CuO-Mg-PVA > CuO-Mg > CuO. Due to the improved catalytic efficiency of MCP expanded with

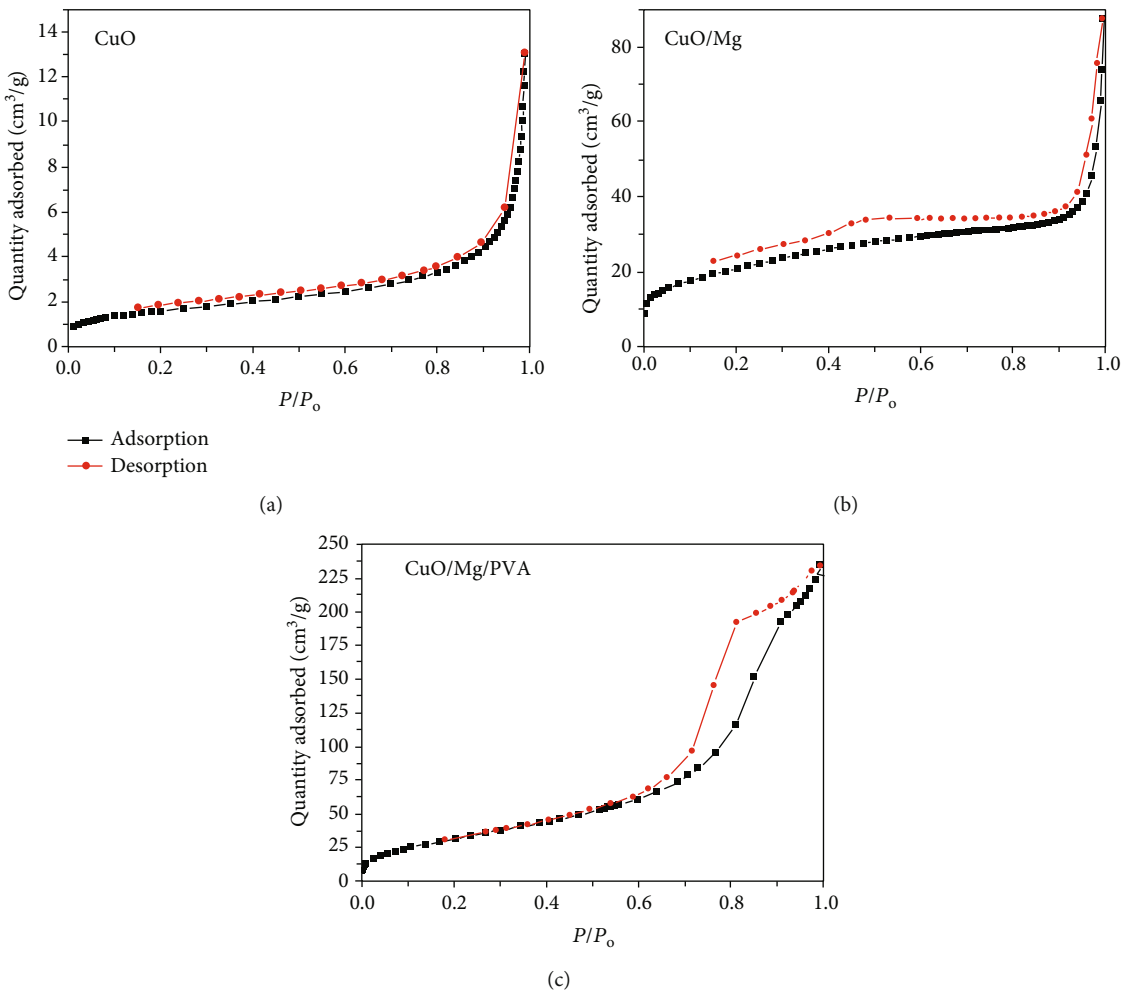


Figure 10: BET $N_2$ adsorption-desorption measurement of (a) CuO, (b) MC, and (c) MCP nanocomposites.

Mg doping, the % of behaviour of the aforesaid catalyst falls in the direction of 95.71%, 80.53%, and 49.72%, respectively. Furthermore, PVA's distinct adsorptive activity and wider intermolecular space were mostly responsible for the significant augmentation of MCP nanocomposite [43]. In comparison to the other samples CuO and MC, the combined impact of Mg and PVA modified with CuO nanoparticles generates an astounding photocatalytic efficiency. Furthermore, the results of the blank studies to assess the effect of photolysis on MB were found to be minimal (8%). The obtained results of degradation of organic dye compared with the already reported values are given in Table 1. Among the reported values, CuO/Mg/PVA nanocomposite shows higher efficiency of degradation of organic dye.

The computation of the potential level of band edge for the two semiconductors is essential in the determination of the photoexcited charge transporter in the coupled/doped semiconductor. The valance band (VB) and conduction band (CB) edge position of MCP nanocomposite can be quantified by the accompanying equation.

$$E_{VB} = X - E_e + 0.5\,E_g, \tag{4}$$

$$E_{CB} = E_g - E_{VB}, \tag{5}$$

where $X$ refers to absolute electronegativity, stated as the geometric mean of the absolute electronegativity of the constituent atoms, which is represented by the arithmetic mean of the atomic electron affinity and 1st I.E. $E_{VB}$ indicates the energy of VB edge potential, $E_{CB}$ is the CB edge potential, $E_g$ stands for band gap energy of the semiconductors, and $E_e$ is nothing but free electron on the H scale (~4.5 eV). Consequently, the band edge potential of $E_{VB}$ and $E_{CB}$ of MCP nanocomposite area unit is computed to be 3.21 and 0.93 eV, severally.

For the improved photocatalytic movement of MCP nanocomposite, the following mechanism has been proposed. Figure 12 shows a schematic picture of photodegradation of MB in MCP nanocomposite caused by sun radiation. The breakdown of MB under solar light illumination was used to assess MCP's increased photocatalytic activity [63]. Because prior studies [64, 65] found that sunlight was more effective than alternative irradiation strategies for dye degradation. When the photocatalyst is illuminated by solar light, PVA modified on the surface of CuO-Mg can be simply excited and generate portable

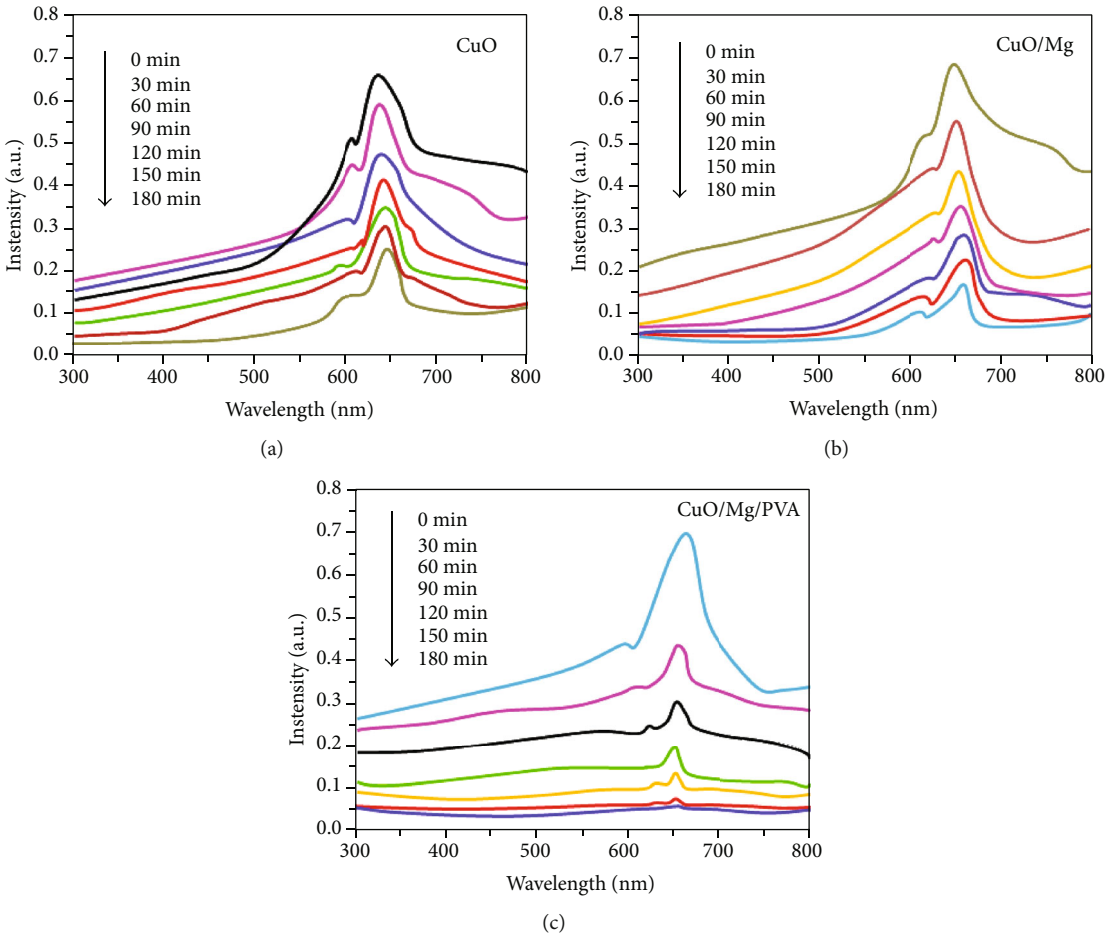


Figure 11: Time-dependent UV-vis spectral change of methylene blue in the presence of (a) CuO, (b) MC, and (c) MCP nanocomposite.

Table 1: Comparative list of the percentage of degradation towards the organic dye.

| S. no | Sample | Degradation % | Dye | Ref |
|---|---|---|---|---|
| 1 | Mo/CuO | 90.0 | Methylene blue | [55] |
| 2 | Ag/$SnO_2$ | 85.0 | Rose bengal | [56] |
| 3 | CuO/ZnO | 93.8 | Methylene blue | [57] |
| 4 | CuS/CuO/cu | 87.4 | Methylene blue | [58] |
| 5 | Cu/$TiO_2$ | 95.0 | Methylene blue | [59] |
| 6 | $NiWO_4$ | 83.0 | Rhodamine B | [60] |
| 7 | MgO | 80.0 | Alizarin red S | [61] |
| 8 | MgO | 75.0 | Methylene blue | [62] |
| 9 | CuO/mg/PVA | 95.7 | Methylene blue | This work |

electrons, which are then introduced into the CB of CuO. In MCP nanocomposite, Mg and PVA perform an electron trap and subsequently accelerate the introduced electrons into surface which adsorbed $O_2$ diminishing $O_2$ to $O^{2\bullet-}$[29]. This consequences in the creation of numerous reactive oxygen species ($O_2^{\bullet-}$ and $^{\bullet}OH$), which stimulates the destruction of MB. The benefit of PVA and Mg doping is that it improves electron-hole segregation and increases quantum yield by accelerating electrons from the catalyst to molecular oxygen quickly.

*3.8.1. Effect of pH.* The pH of the solution is a significant factor that determines dye molecule adsorption. The surface charge of the nanocomposite can influenced by pH changes. The degree of ionization of the adsorbate molecule and the surface behaviour of the adsorbent are affected by the pH solution and variations in pH cause variations in the degree of ionization of the adsorbate molecule and the surface behaviour of the adsorbent [66]. At 30°C, the consequence of pH solution on dye adsorption was investigated by maintaining the dye concentration at 3 $\mu$M and the adsorbent dosage at 0.05 g/L. The experiment was carried out with pH levels ranging from 3 to 9. The outcomes are depicted in Figure 13. The percentage of dye elimination increased consistently from 80.23% to 96.18% with a change in pH

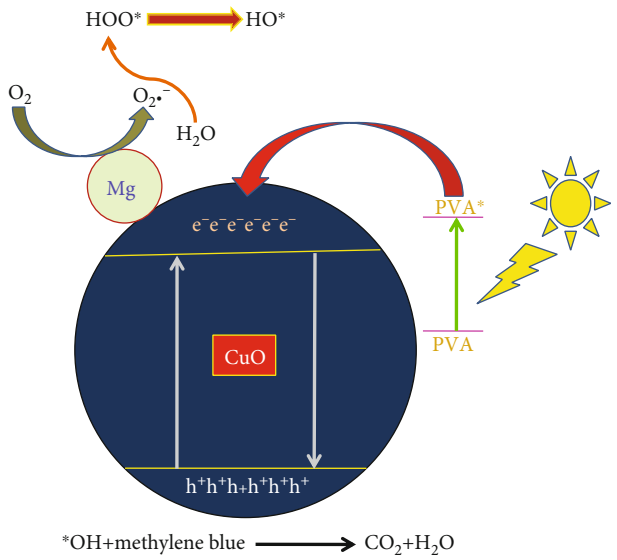


Figure 12: Mechanism of methylene blue degradation.

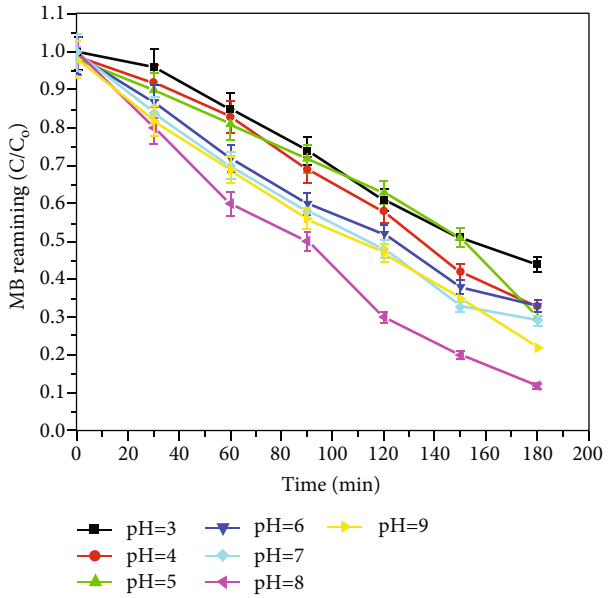


Figure 13: Effect of pH on the photodegradation of MB.

from 3 to 8 attributable to the better electrostatic interaction between the positively charged dye molecule and contrarily charged nanocomposite. Beyond the pH 9, removal of dye decreased to 90.75%, this is owing to the change in electrostatic fascination or aversion between MB and catalyst, and hence, the optimal pH for degradation dye MB was set to be 8.

*3.8.2. Effect of Photocatalyst Dosage.* The effect of photocatalyst dosage was also investigated to find the optimal dosage of MCP nanocomposite by adjusting the catalyst dosage from 0.1 to 0.4 g/L while maintaining the MB concentration at 3 $\mu$M. The outcomes are exhibited in Figure 14. When the photocatalyst dosage is enlarged from 0.1 to 0.3 g/L, the photodegradation of MB rises. When more photons are

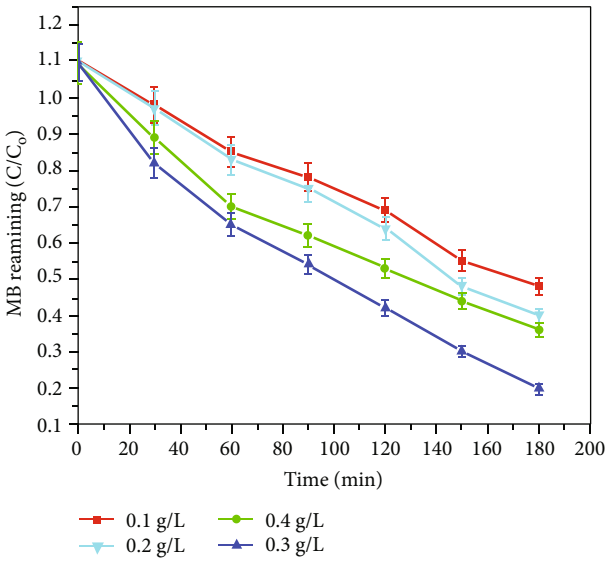


Figure 14: Effect of catalyst dosage on the photodegradation of MB.

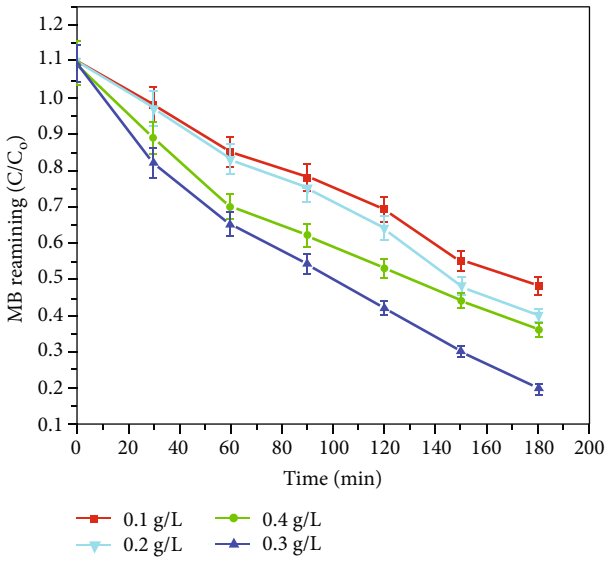


Figure 15: Effect of concentration on the photodegradation of MB.

adsorbed and highly reactive oxygen species ($O^2$•- and •OH) are generated for photodegradation, the accessibility of the absolute surface region and active sites of the catalyst increases. Nevertheless, photodegradation tendency diminished at large photocatalyst dosage (beyond 0.3 g/L) owing to the deficit of surface area and active sites manipulated by agglomeration of nanoparticles as well as an increase in the obscurity of the suspension, which drives infiltration of light via the solution. Thus, only a lesser number of photons will meet the catalyst surface. Hence, the creation of reactive oxygen species is most extreme; therefore, the photocatalytic performance is shriveled.

*3.8.3. Effect of Dye Concentration.* The various initial concentration of MB dye was investigated in the range of 0.3

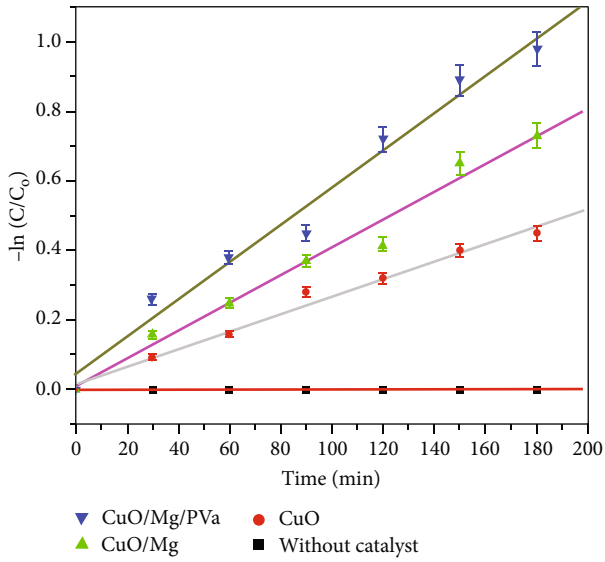


FIGURE 16: Kinetic plot of $-\ln(C/C_o)$ versus irradiation time for the photodegradation of MB.

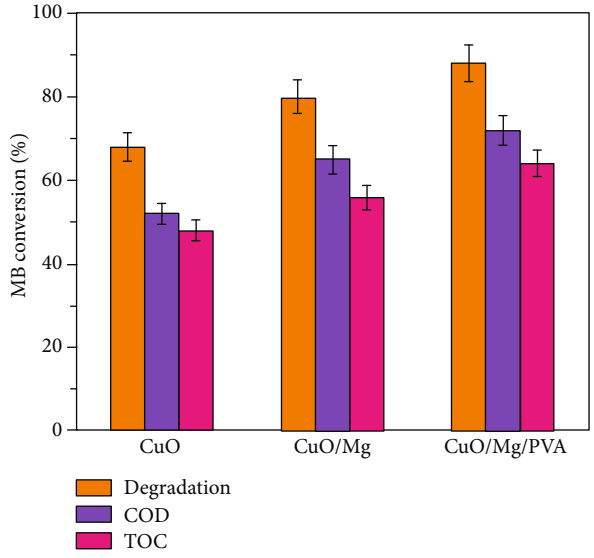


FIGURE 17: Comparison of photodegradation and COD and TOC removal percentage of MB in the presence of CuO, Mg-CuO, and Mg/CuO/PVA nanocomposites.

to 0.6 $\mu$M under ideal pH of 8 and the catalyst dosage of 0.2 g/L. The consequences are presented in Figure 15. It is seen that the photodegradation % of MB diminished with an increment in MB concentration. It tends to be clarified dependent on Beer-Lambert's law. As indicated by the law, the pathway length of photons incoming into the sample diminished with expanding of MB concentration, and trivial photons approach the surface of the catalyst. Many MB species are adsorbed on the catalyst surface when the MB dye concentration was higher. As a result, MB molecules completely ring the active places on the catalytic surface. From the outcomes, as the dye concentration grew, the photodegradation efficiency declined. The optimal initial

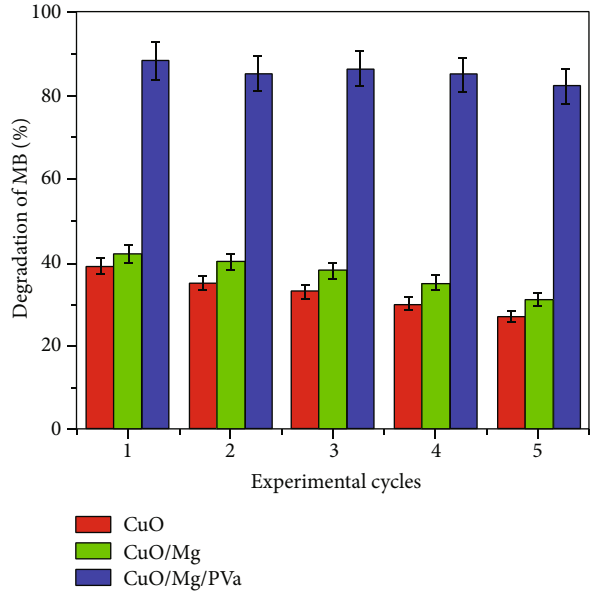


FIGURE 18: Cycling runs for photocatalytic degradation of MB over MCP nanocomposite under solar light irradiation.

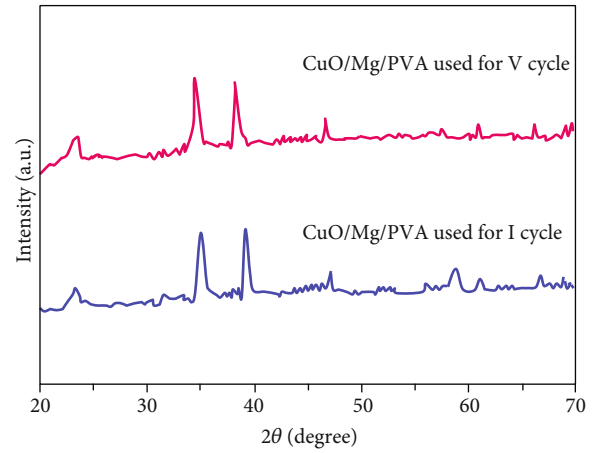


FIGURE 19: XRD patterns of MCP nanocomposite before and after five consecutive photocatalytic reactions.

MB concentration of 0.3 $\mu$M is achieved for improved photodegradation of MB.

*3.8.4. Kinetic of MB Photodegradation.* The kinetic of MB degradation under solar light for CuO, MC, and MCP nanocomposites was analyzed. The degradation proficiency of MB dye is quantified by utilizing the Langmuir-Hinshelwood formula.

$$-\ln(C/C_o) = kt, \tag{6}$$

where $C_o$ is the initial concentration of MB at t zero min and $C$ is that the concentration of MB at illumination time "$t$" is portrayed in Figure 16. From Figure 16, photodegradation reaction implies pseudo 1$^{st}$-order kinetics. The corresponding

rate constant ($k$) for the photocatalytic decoloration of MB was determined. The calculated rate constants for CuO, MC, and MCP nanocomposites are $3.91 \times 10^{-4}\,S^{-1}$, $2.34 \times 10^{-3}\,S^{-1}$, and $1.22 \times 10^{-3}\,S^{-1}$, respectively. The MCP nanocomposite exhibits brilliant photocatalytic behaviour towards the damage of MB rather than that of CuO and MC nanoparticles.

*3.8.5. TOC and COD Measurement.* To track the toxicity of the photodegradation dye solution, TOC and COD analyses were conducted. The outcomes are revealed in Figure 17. MCP nanocomposite outperformed all other photocatalysts in terms of removing the most TOC, COD, and degradation. The maximal deterioration, COD, and TOC, respectively, are 88%, 72%, and 64%. The explanation for the modest quantity of TOC and COD removal in organic dyes is that more organic dyes are mineralized during the photocatalytic process.

*3.8.6. Repeatability and Reusability.* Because of the fundamental characteristic of a brilliant catalyst and any possible saturation influence, the same catalyst is employed by photocatalytic decoloration consistently, and reusability and stability are other important aspects for practical use. Figure 18 illustrates the percentage of MB degradation vs. experimental cycles of CuO, MC, and MCP nanocomposites, which were analyzed for 5 cycles to constant catalyst infinite quality (0.2 g/L) at ideal pH. The photocatalytic activity of M6P did not alter much. Even after five cycles, the degradation percentage of MB is above 80%. Because of the high charge separation efficiency of PVA and Mg on CuO nanoparticles, M6P nanocomposite has superior catalytic activity than other components. The XRD pattern of the M6P nanocomposite (Figure 19) was examined after the consecutive cycles. The M6P nanocomposite remained untouched. As a result, the M6P photocatalyst can remain stable throughout photocatalytic damage of MB in the existence of solar light.

## 4. Conclusion

Novel sun-powered light-driven CuO/Mg/PVA nanocomposite was prepared successfully by combined sonochemical synthesis and chemical impregnated route. Interfacial modifiers such as Mg and PVA have little effect on the crystal structure, as shown by XRD patterns and SEM data. The presence of Cu and Mg elements was confirmed by EDX spectra. Under solar light illumination, the CuO/Mg/PVA nanocomposite exhibits unique photocatalytic characteristics. The photocatalytic degradation of MB has been determined to be 95.71 percent efficient. CuO/Mg/PVA nanocomposite has increased photocatalytic activity owing to the reduction of electron-hole reunion in CuO through PVA and Mg. The photocatalytic destruction of MB under solar light has been presented as a plausible mechanism. The reaction parameters have been tuned, resulting in maximal photocatalytic degradation. Furthermore, the photocatalyst CuO/Mg/PVA nanocomposite is proven by XRD analysis to be steady without dissipating of action even later 5 cycle investigation. The results show that all these properties are improved after doping CuO with Mg and PVA. Among all the three samples, CuO/Mg/PVA nanocomposite has demonstrated an excellent photocatalytic performance in the degradation of MB dye. Hence, this sample can be ideally employed for the purification of water by degrading the methylene blue present in it.

## Data Availability

All relevant data are included within the article.

## Disclosure

This paper was performed as part of the employment of the authors.

## Conflicts of Interest

All authors declare that there is no conflict of interest.

## Acknowledgments

MSK acknowledges the generous support from the Research Supporting Project (RSP-2021/352) by the King Saud University, Riyadh, Kingdom of Saudi Arabia.

## References

[1] A. Roy, A. Sharma, S. Yadav, L. T. Jule, and R. Krishnaraj, "Nanomaterials for remediation of environmental pollutants," *Bioinorganic Chemistry and Applications*, vol. 2021, 16 pages, 2021.

[2] N. Aziz, M. Faraz, R. Pandey et al., "Facile algae-derived route to biogenic silver nanoparticles: synthesis, antibacterial, and photocatalytic properties," *Langmuir*, vol. 31, no. 42, pp. 11605–11612, 2015.

[3] A. Roy, A. Elzaki, V. Tirth et al., "Biological synthesis of nanocatalysts and their applications," *Catalysts*, vol. 11, no. 12, p. 1494, 2021.

[4] C. Pandit, A. Roy, S. Ghotekar et al., "Biological agents for synthesis of nanoparticles and their applications," *Journal of King Saud University-Science*, vol. 34, no. 3, article 101869, 2022.

[5] A. Roy, H. A. Murthy, H. M. Ahmed, M. N. Islam, and R. Prasad, "Phytogenic synthesis of metal/metal oxide nanoparticles for degradation of dyes," 2021.

[6] C. M. Gao, T. Wei, Y. Y. Zhang et al., "A photoresponsive rutile $TiO_2$ heterojunction with enhanced electron hole separation for high-performance hydrogen evolution," *Advanced Materials*, vol. 8, article 1806596, 2019.

[7] G. J. Zhai, J. G. Wang, Z. M. Chen, S. F. Yang, and Y. Men, "Highly enhanced soot oxidation activity over 3DOM $Co_3O_4$ – $CeO_2$ catalysts by synergistic promoting effect," *Journal of Hazardous Materials*, vol. 363, pp. 214–226, 2019.

[8] R. C. Shen, C. J. Jiang, Q. J. Xiang, J. Xie, and X. Li, "Surface and interface engineering of hierarchical photocatalysts," *Applied Surface Science*, vol. 471, pp. 43–87, 2019.

[9] G. P. Xu, P. R. Anusuyadevi, C. Aymonier, R. Luque, and S. Marre, "Nanostructured materials for photocatalysis," *Chemical Society Reviews*, vol. 48, no. 14, pp. 3868–3902, 2019.

[10] E. Abbasi-Asl, M. Haghighi, and A. Talati, "Sono-solvothermal fabrication of flowerlike $Bi_7O_9I_3$-$MgAl_2O_4$ p-n nanoheterostructure photocatalyst with enhanced solar-light-

driven degradation of methylene blue," *Solar Energy*, vol. 184, pp. 426–439, 2019.

[11] G. H. Oliveira, M. T. Galante, T. T. Martins et al., "Real time single $TiO_2$ nanoparticle monitoring of the photodegradation of methylene blue," *Solar Energy*, vol. 190, pp. 239–245, 2019.

[12] A. Lebedev, G. H. H. Ma, F. Anariba et al., "Design and fabrication of BiV (O, N)$_4$ p-n homojunction solid solutions for enhanced methylene blue degradation via LED light irradiation," *Solar Energy*, vol. 160, pp. 298–302, 2018.

[13] M. S. Hosseini, M. Ebratkhahan, Z. Shayegan et al., "Investigation of the effective operational parameters of self-cleaning glass surface coating to improve methylene blue removal efficiency; application in solar cells," *Solar Energy*, vol. 207, pp. 398–408, 2020.

[14] A. M. Azharudeen, T. Suriyakala, M. Rajarajan, and A. Suganthi, "An improved sensitive and selective non-enzymatic glucose sensor based on PEG assisted CuO nanocomposite," *Egyptian Journal of Chemistry*, vol. 62, pp. 487–500, 2019.

[15] N. H. Deepthi, Y. S. Vidya, K. S. Anantharaju et al., "Optical, electrical and luminescent studies of CuO/MgO nanocomposites synthesized via sonochemical method," *Journal of Alloys and Compounds*, vol. 786, pp. 855–866, 2019.

[16] X. Jin, F. Chen, D. Jia et al., "Influences of synthetic conditions on the photocatalytic performance of ZnS/graphene composites," *Journal of Alloys and Compounds*, vol. 280, pp. 299–305, 2019.

[17] L. Wu, Y. Wang, P. Li et al., "Enhanced nonlinear optical behavior of graphene-CuO nanocomposites investigated by Z-scan technique," *Journal of Alloys and Compounds*, vol. 777, pp. 759–766, 2019.

[18] Y. X. Gu, Y. X. Xuan, H. Zhang, X. Y. Deng, M. J. Bai, and L. Wang, "A facile coordination precipitation route to prepare porous CuO microspheres with excellent photo-Fenton catalytic activity and electrochemical performance," *CrystEngComm*, vol. 21, no. 4, pp. 648–655, 2019.

[19] Y. G. Sun, L. Y. Cai, X. J. Liu, Z. Cui, and P. H. Rao, "Tailoring heterostructures of Ag/$Cu_2O$ hybrids for enhanced photocatalytic degradationdegradation," *Journal of Physics and Chemistry of Solids*, vol. 111, pp. 75–81, 2017.

[20] J. Zaho, C. C. Zhang, and D. B. Wang, "A facile one-step synthesis of p-CuO/n-ZnO nanowire heterojunctions by thermal oxidation route," *Materials Science in Semiconductor Processing*, vol. 35, pp. 55–58, 2015.

[21] C. H. Feng, X. P. Meng, X. L. Song, X. T. Feng, Y. Zhao, and G. Liu, "Controllable synthesis of hierarchical CuS/ZnS hetero-nanowires as high-performance visible-light photocatalysts," *RSC Advances*, vol. 6, no. 111, pp. 110266–110273, 2016.

[22] C. Xu, K. V. Manukyan, R. A. Adams, V. G. Pol, P. Chen, and A. Varma, "One-step solution combustion synthesis of CuO/$Cu_2O$/C anode for long cycle life Li-ion batteries," *Carbon*, vol. 142, pp. 51–59, 2019.

[23] S. S. G. Srinivasan, B. Govardhanan, P. Aabel, M. Ashok, and M. C. Santhoshkumar, "Effect of oxygen partial pressure on the tuning of copper oxide thin films by reactive sputtering for solar light driven photocatalysis," *Solar Energy*, vol. 187, pp. 368–378, 2019.

[24] K. Sahu, S. Choudhary, and S. Mohapatra, "Fabrication of Au-CuO hybrid plasmonic nanostructured thin films with enhanced photocatalytic activity," *Materials Research Bulletin*, vol. 123, p. 110707, 2020.

[25] S. Raina, A. Roy, and N. Bharadvaja, "Degradation of dyes using biologically synthesized silver and copper nanoparticles," *Environmental Nanotechnology, Monitoring & Management*, vol. 13, p. 100278, 2020.

[26] Y. Keriti, R. Brahimi, Y. Gabes, S. Kail, and M. Trari, "Physical and photo-electrochemical properties of CuO thin film grown on $\mu$C-Si: H/glass. Application to solar energy conversion," *Solar Energy*, vol. 206, pp. 787–792, 2020.

[27] M. L. Ovcharov, A. M. Mishura, N. D. Shcherban, S. M. Filonenco, and V. M. Granchak, "Photocatalytic reduction of $CO_2$ using nanostructured $Cu_2O$ with foam-like structure," *Solar Energy*, vol. 139, pp. 452–457, 2016.

[28] A. P. Wanninayaki, B. C. Church, and N. Abuzahra, "Annealing effect on ZnO-NPs buffer layer assembled organic solar cells synthesized with CuO nanoparticles," *Advanced Materials Letters*, vol. 8, no. 1, pp. 8–12, 2017.

[29] M. Sun, Y. Lei, H. Cheng et al., "Mg doped CuO-$Fe_2O_3$ composites activated by persulfate as highly active heterogeneous catalysts for the degradation of organic pollutants," *Journal of Alloys and Compounds*, vol. 825, p. 154036, 2020.

[30] N. C. S. Selvam, S. Narayanan, L. J. Kennedy, and J. J. Vijaya, "Pure and Mg-doped self-assembled ZnO nano-particles for the enhanced photocatalytic degradation of 4-chlorophenol," *Journal of Environmental Sciences*, vol. 25, no. 10, pp. 2157–2167, 2013.

[31] W. Bai, X. Yang, X. Du et al., "Robust and recyclable macroscopic g-$C_3N_4$/cellulose hybrid photocatalysts with enhanced visible light photocatalytic activity," *Applied Surface Science*, vol. 504, p. 144179, 2020.

[32] A. M. Azharudeen, R. Karthiga, M. Rajarajan, and A. Suganthi, "Enhancement of electrochemical sensor for the determination of glucose based on mesoporous $VO_2$/PVA nanocomposites," *Surfaces and Interfaces*, vol. 16, pp. 164–173, 2019.

[33] Y. Yang, Z. Chen, X. Wu, X. Zhang, and G. Yuan, "Nanoporous cellulose membrane doped with silver for continuous catalytic decolorization of organic dyes," *Cellulose*, vol. 25, no. 4, pp. 2547–2558, 2018.

[34] G. Jyoti, A. Keshav, and J. Anandkumar, "Esterification of acrylic acid with ethanol using pervaporation membrane reactor," *Korean Journal of Chemical Engineering*, vol. 34, no. 6, pp. 1661–1668, 2017.

[35] A. Shameli and E. Ameri, "Synthesis of cross-linked PVA membranes embedded with multi-wall carbon nanotubes and their application to esterification of acetic acid with methanol," *Chemical Engineering Journal*, vol. 309, pp. 381–396, 2017.

[36] Y. K. Lin, V. H. Nguyen, J. C. C. Yu et al., "Biodiesel production by pervaporation-assisted esterification and pre-esterification using graphene oxide/chitosan composite membranes," *Journal of the Taiwan Institute of Chemical Engineers*, vol. 79, pp. 23–30, 2017.

[37] D. Unlu and N. D. Hilmioglu, "Pervaporation catalytic membrane reactor application over functional chitosan membrane," *Journal of Membrane Science*, vol. 559, pp. 138–147, 2018.

[38] J. Ayhan, P. Bayram, C. Zeki, and A. Recai, "Biofilms from micro/nanocellulose of $NaBH_4$ modified kraft pulp," *Bulletin of Materials Science*, vol. 40, no. 4, pp. 699–710, 2017.

[39] J. Lv, G. Zhang, H. Zhang, C. Zhao, and F. Yang, "Improvement of antifouling performances for modified PVDF ultrafiltration membrane with hydrophilic cellulose nanocrystal," *Applied Surface Science*, vol. 440, pp. 1091–1100, 2018.

[40] A. M. Alamaria, M. G. M. Nawawi, and Z. Zamrud, "Sago/PVA blend membranes for the recovery of ethyl acetate from water," *Arabian Journal of Chemistry*, vol. 12, no. 8, pp. 2183–2191, 2019.

[41] Y. Song, J. Zhang, H. Yang, S. Xu, L. Jiang, and Y. Ban, "Preparation and visible light-induced photo-catalytic activity of H-PVA/$TiO_2$ composite loaded on glass via sol-gel method," *Applied Surface Science*, vol. 292, pp. 978–985, 2014.

[42] S. Li, G. Li, Q. Chen, and F. Wang, "Facile green synthesis of degraded PVA coated $TiO_2$ nanoparticles with enhanced photocatalytic activity under visible light," *Journal of Physics and Chemistry of Solids*, vol. 129, pp. 92–98, 2019.

[43] E. Filippo, C. Carlucci, A. L. Capodilupo et al., "Facile preparation of TiO2-polyvinyl alcohol hybrid nanoparticles with improved visible light photocatalytic activity," *Applied Surface Science*, vol. 331, pp. 292–298, 2015.

[44] Z. Liu, R. Liu, Y. Yi, W. Han, F. Kong, and S. Wang, "Photocatalytic degradation of dyes over a xylan/PVA/$TiO_2$ composite under visible light irradiation," *Carbohydrate Polymers*, vol. 223, pp. 115081–115088, 2019.

[45] T. Jan, J. Iqbal, V. Farooq et al., "Structural, Raman and optical characteristics of Sn doped CuO nanostructures: a novel anticancer agent," *Ceramics International*, vol. 41, no. 10, pp. 13074–13079, 2015.

[46] O. Rezaee, H. M. Chenari, F. E. Ghodsi, and H. Ziyadi, "Preparation of PVA nanofibers containing tungsten oxide nanoparticle by electrospinning and consideration of their structural properties and photocatalytic activity," *Journal of Alloys and Compounds*, vol. 690, pp. 864–872, 2017.

[47] F. Bayansal, O. Sachin, and H. W. Cetikare, "Mechanical and structural properties of Li-doped CuO thin films deposited by the successive ionic layer adsorption and reaction method," *Thin Solid Films*, vol. 697, p. 137839, 2020.

[48] Y. F. Zhang, M. M. Guo, Y. Zhang et al., "Flexible, stretchable and conductive PVA/PEDOT:PSS composite hydrogels prepared by SIPN strategy," *Polymer Testing*, vol. 81, pp. 106213–106218, 2020.

[49] H. Zhang and J. Zhang, "The preparation of novel polyvinyl alcohol (PVA)-based nanoparticle/carbon nanotube (PNP/CNTs) aerogel for solvents adsoption application," *Journal of Colloid and Interface Science*, vol. 569, pp. 264–266, 2020.

[50] T. Jiang, Y. Zhao, M. Liu, Y. Chen, Z. Xia, and H. Xu, "Enhancing the lifetime of photoinduced charge carriers in $CuFeO_2$ nanoplates by hydrothermal doping of Mg for photoelectrochemical water reduction," *Physica Status Solidi (a)*, vol. 215, article 1800056, 2018.

[51] M. Ahamed, E. Ahamed, Z. L. Hong, X. L. Jiao, T. Abbas, and N. R. Khalid, "Enhancement in visible light-responsive photocatalytic activity by embedding Cu-doped ZnO nanoparticles on multi-walled carbon nanotubes," *Applied Surface Science*, vol. 285, pp. 702–712, 2013.

[52] C. Kuang, S. Wang, M. Luo, J. Cai, and J. Zhao, "Investigation of CuO-based oxygen carriers modified by three different ores in chemical looping combustion with solid fuels," *Renewable Energy*, vol. 154, pp. 937–948, 2020.

[53] G. Eshaq, A. M. Rabie, A. A. Bakr, A. H. Mady, and A. E. Elmetwally, "Cr (VI) adsorption from aqueous solutions on to Mg-Zn-Al LDH and its corresponding oxide," *Desalination and Water Treatment*, vol. 57, pp. 1–11, 2015.

[54] H. K. Melvinng and C. P. Leo, "Translucent and adsorptive PVA thin film containing microfibrillated cellulose intercalated with $TiO_2$ nanoparticles for dye removal," *Colloids and Surfaces, A: Physicochemical and Engineering Aspects*, vol. 578, article 123590, 2019.

[55] M. Maraj, A. Raza, X. Wang, J. Chen, K. N. Riaz, and W. Sun, "Mo-doped CuO nanomaterial for photocatalytic degradation of water pollutants under visible light," *Catalysts*, vol. 11, pp. 1198/1–1198/10, 2021.

[56] K. Vignesh, R. Hariharan, M. Rajarajan, and A. Suganthi, "Photocatalytic performance of Ag doped $SnO_2$ nanoparticles modified with curcumin," *Solid State Sciences*, vol. 21, pp. 91–99, 2013.

[57] K. Sahu, A. Bisht, S. Kuriakose, and S. Mohapatra, "Two-dimensional CuO-ZnO nanohybrids with enhanced photocatalytic performance for removal of pollutants," *Journal of Physics and Chemistry of Solids*, vol. 137, p. 109223, 2020.

[58] C. Wu, Y. Sun, Z. Cui, F. Song, and J. Wang, "Fabrication of Cus/CuO nanowire heterostructures on copper mesh with improved visible light photocatalytic properties," *Journal of Physics and Chemistry of Solids*, vol. 140, p. 109355, 2020.

[59] F. Gao, J. Jiang, L. Du, X. Liu, and Y. Ding, "Stable and highly efficient cu/$TiO_2$ nanocomposite photocatalyst prepared through atomic layer deposition," *Applied Catalysis A: General*, vol. 568, pp. 168–175, 2018.

[60] M. Hao, X. Mang, and Y. Miao, "Synthesis of $NiWO_4$ powder crystals of polyhedron for photocatalytic degradation of rhodamine," *Solid State Sciences*, vol. 72, pp. 103–108, 2017.

[61] R. Taourasi, M. Khaddor, A. Laghzal, and A. E. Kasmi, "Facile one-step synthesis of highly efficient single oxide nanoparticles for photocatalytic application," *Scientific African*, vol. 8, article e00305, 2020.

[62] G. Balakrishnan, R. Velavan, K. M. Batoo, and E. H. Raslan, "Microstructure, optical and photocatalytic properties of MgO nanoparticles," *Results in Physics*, vol. 16, article 103013, 2020.

[63] A. Raja, S. Ashokkumar, R. M. Pavithra et al., "Eco friendly preparation of zinc oxide nanoparticles using Tabernaemontane divaricata and its photocatalytic and antimicrobial activity," *Journal of Photochemistry and Photobiology B*, vol. 181, pp. 53–58, 2018.

[64] M. Ropisah, W. S. Mohd, B. D. Laily, A. Azizan, I. Nazlina, and N. A. A. Siti, "Synthesis of silver nanoparticles with anti microbial activity using the lichen parmotrema praesorediosum," *International Journal of Nanomedicine*, vol. 9, no. 1, pp. 121–134, 2014.

[65] V. Badineni, H. Maseed, S. K. Arta, S. Yerramala, B. V. Kumarnaidu, and K. Kaviyarasu, "Effect of PVA/PVP Protective Agent on the Formation of Silver nanoparticles and its photocatalytic and Antimicrobial Activity," *Materials Today: Proceedings*, vol. 36, pp. 121–125, 2021.

[66] P. K. Jaseela, J. Garvasis, and A. Joseph, "Selective adsorption of methylene blue (MB) dye from aqueous mixture of MB and methyl orange (MO) using mesoporous titania ($TiO_2$)-poly vinyl alcohol (PVA) nanocomposite," *Journal of Molecular Liquids*, vol. 286, pp. 110908–110910, 2019.